ACS OMEGA

Open Access

http://pubs.acs.org/journal/acsodf

Article

Fast Synthesis of Biochar by Hydrolysis with an Acid Catalyst for Efficient Low-Temperature SCR of NO

Fan Li, Junchao Xu,* Yiming Xie,* Qingdong Yao, Fangyue Hu, Li Lv, and Huaqiang Chu

Cite This: https://doi.org/10.1021/acsomega.5c04370

Read Online

ACCESS | Metrics & More | Article Recommendations

ABSTRACT: Biochar stands out as an excellent carrier for low-temperature SCR catalysts, but its synthesis is often time-consuming and requires high temperatures and fossil fuels. Therefore, sustainable and rapid synthesis methods are challenged. This paper proposes a sustainable method for the rapid synthesis of rice husk biochar by acid-catalyzed hydrolysis at ambient temperature and pressure. The results showed that the surface of the biochar synthesized by acid-catalyzed hydrolysis was smooth, and also the SiO_2 powder byproduct with uniform particle size was successfully obtained. Furthermore, a biochar carrier-based SCR catalyst was developed. The product demonstrated exceptional low-temperature denitrification performance with a denitrification efficiency of 96.8% at 180 °C. Notably, the product synthesis required a shorter time and exhibited higher denitrification efficiency and a wider temperature range than the biochar prepared by pyrolysis and chemical activation. Thus, acid-catalyzed hydrolysis proved to be a simple, low-energy, and sustainable method for producing high-quality biochar.

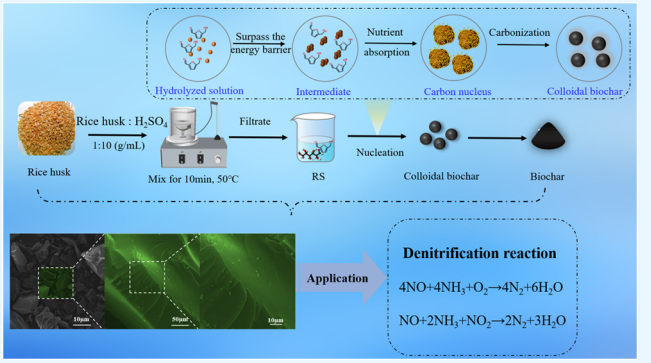

1. INTRODUCTION

The synthesis and application of carbon materials have a long history.[1] Beginning with the discovery and application of fullerenes[2] in 1985 and carbon nanotubes[3] in 1991, research related to carbon materials has become a popular area with potential applications, including catalyst carriers,[4] adsorbents,[5] supercapacitors,[6] sensors,[7] and electrodes.[8]

According to the structural characteristics and component features of the biocarbon precursors, different synthetic routes should be adopted.[9] Plant- and animal-based precursors have large molecular weights and generally follow a "top-down" synthetic route, which requires a step to break down the macromolecules during the synthesis process. The key process is how to efficiently reduce the particle size of biomass through physical and chemical means after carbonization. Carbohydrate-type biocarbon usually adopts a "bottom-up" synthetic route, and the products present a smooth spherical structure and excellent purity and uniformity but have a low pore size distribution and specific surface area. Xu et al.[10] provided a detailed review of the latest research progress in the synthesis methods, energy consumption, and application of biomass charcoal. In practical terms, synthesis methods of carbon materials include chemical vapor deposition,[11] arc discharge,[12] mechanical ball milling,[13] and microwave-assisted pyrolysis,[14] which are mainly used to synthesize amorphous, porous, or crystalline carbon with different sizes, shapes, and chemical compositions.[15,16]

However, the above-mentioned synthesis methods are usually cumbersome and time-consuming and require the use of organic solvents and post-treatment.[10] Furthermore, these processes often rely on expensive fossil fuels, metal catalysts, and complex devices with high temperatures and pressures, which are environmentally and economically unsustainable, limiting the low-energy production and application of carbon materials.[17] To reduce energy consumption as well as the environmental pollution generated by synthesizing carbon materials, the current research direction tends to shift the carbon source to environmentally friendly biomass resources, including plants and animals,[18] lignin,[19] polysaccharides[20] (cellulose, starch, and sucrose), and monosaccharides[21] (glucose, fructose, and xylose) and to replace high-energy-consuming synthesis equipment with low-energy-consuming equipment. For example, Wang et al.[22] prepared biomass carbon for gas separation and supercapacitors by combining potassium hydroxide (KOH) activation with pyrolysis using algae as a carbon source; Zhang et al.[23] prepared heteroatom-

Received: May 12, 2025
Revised: June 26, 2025
Accepted: July 7, 2025

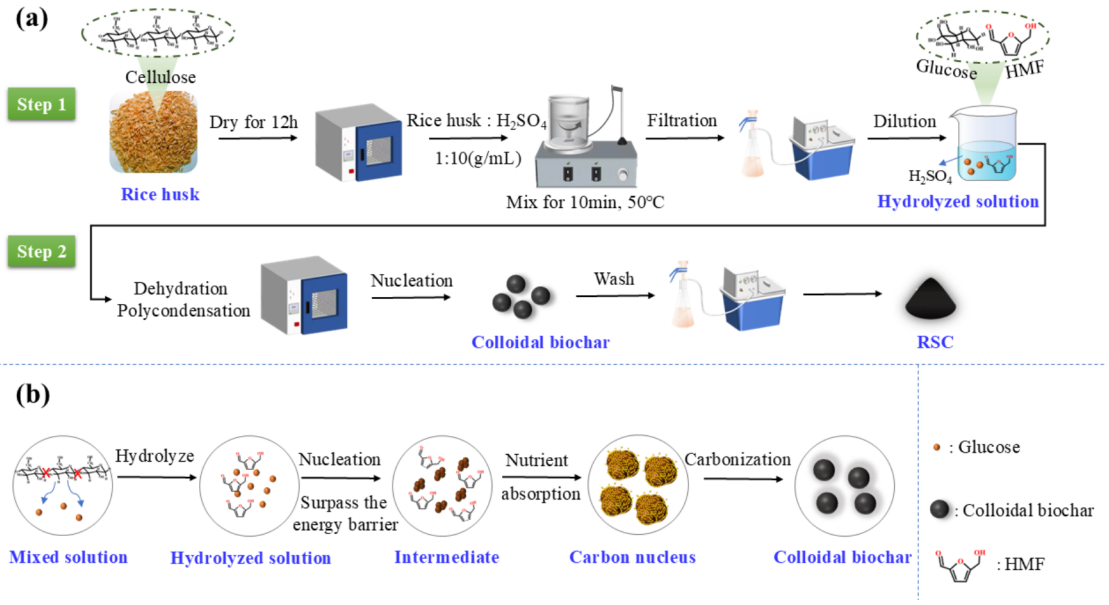

Figure 1. (a) RSC synthesis; (b) synthesis mechanism of colloidal biochar.

doped biomass carbon to catalyze oxidative redox reactions by using shrimp shells as a carbon source and using a mechanical ball milling method + chemical activation; and Guo et al.[24] used pig blood as a carbon source and prepared biomass carbon for catalytic oxidative redox reactions by pyrolysis method with heat treatment at 350 °C for 6 h followed by ball milling method. However, the synthesis of biomass carbon in the above studies still has the disadvantages of a complicated preparation process, slow speed, high energy consumption, and the need for post-treatment.

Rice husk, which contains 30 wt % of cellulose and about 41% of elemental C, is considered as one of the potential raw materials for activated carbon preparation. The current annual global rice production is about 477 million tons,[25] making rice husk a cheap and easily available biomass carbon source. The commonly used methods to synthesize carbon materials from biomass include pyrolysis,[26] templating,[27] solvothermal,[28] and activation.[29] Among them, acid-catalyzed hydrolysis belongs to one kind of solvent method that possesses the advantages of simple equipment, relatively fast synthesis, mild conditions (ordinary temperature and pressure), and low energy consumption. It is a method of biochar synthesis that is worth further study.

Selective catalytic reduction (SCR) is an effective technology to reduce NO_X emissions, and ammonia (NH_3)-SCR has been widely used in domestic and international industries due to its high activity efficiency and N_2 selectivity. Currently, commercial catalysts such as vanadium pentoxide-based titanium dioxide formulations (V_2O_5–WO_3/TiO_2, V_2O_5–MoO_3/TiO_2, and V_2O_5/TiO_2) are widely used worldwide. However, these catalysts suffer from high vanadium toxicity, narrow activity temperature windows (300–400 °C), and poor low-temperature SCR activity. This leads to problems such as poor catalyst activity, easy clogging, and a shortened service life. Therefore, simple removal of dust during synthesis can avoid the clogging problem; in addition, Mn and Ce synergistically increase the conversion rate of NO to NO_2, and the abundant pore structure present in the biochar can support the above chemical reactions.

Therefore, acid hydrolysis was used to rapidly synthesize structurally controllable rice husk biochar at ordinary temperatures and pressures in this paper. Meanwhile, SiO_2 powder byproducts with a particle size of about 50 μm were obtained. Subsequently, the synthesized biochar was demonstrated to have an excellent low-temperature denitration performance through the preparation of low-temperature SCR catalysts and performance characterization. In addition, it may be further applied in the fields of catalysis, adsorption, and energy storage.

2. MATERIALS AND METHODS

2.1. Fast Synthesis of Biochar by Hydrolysis with Acid Catalyst. The synthesis of biochar by hydrolysis with an acid catalyst can be divided into two stages: hydrolysis solution and biochar formation, as shown in Figure 1a. Step 1: dried rice husk was mixed with 72% concentration of H_2SO_4 solution at a ratio of 1:10 (g/mL), stirred at 50 °C for 10 min in a magnetic stirrer, and then filtered to remove residual; after that, distilled water was added to dilute the mixed resolution until the concentration of H_2SO_4 was 42%, obtaining hydrolysis solution. Step 2: the hydrolysis solution was placed in a drying oven after 6 h to undergo dehydration, condensation, and carbonization process. Then, the above product was filtrated and washed until neutral and dried at 80 °C to obtain the acid-hydrolyzed biochar, recorded as RSC.

In addition, we list the time required to synthesize biochar by different methods (pyrolysis + chemical vapor deposition,[30] ball milling + pyrolysis,[31] hydrothermal,[32] soft template method,[33] microwave-assisted pyrolysis,[34] and this work), as shown in Figure 2. It can be seen that even without counting the time required for pretreatment, these methods require a longer time for the synthesis process. Furthermore, both in terms of experimental time and energy consumption as well as operational steps, its cost is higher than that of the acid hydrolysis method.

In the above synthesis process, the synthesis mechanism can be divided into the following steps. ① 72% concentration of sulfuric acid hydrolyzed the rice husk to remove hemicellulose, lignin, and metal impurities.[35] ② The H^+ in the hydrolysis

https://doi.org/10.1021/acsomega.5c04370
ACS Omega XXXX, XXX, XXX−XXX

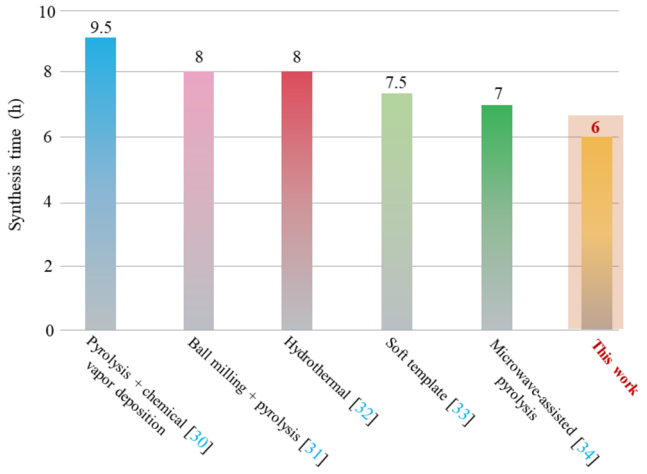

Figure 2. Time required to synthesize biochar was determined by different methods.

solution breaks the glycosidic bonds in cellulose, converting it to glucose and oligomers, and subsequently glucose is converted to 5-hydroxymethylfurfural (HMF) and a variety of aromatic compounds.[36] ③ As the reaction proceeds, the concentration of nutrients continues to energize until the energy barrier is breached and homogeneous nucleation occurs to form carbon core, which further absorbs surrounding nutrients for continued growth. The synthesis mechanism is shown in Figure 1b, which shows that the process is a recombinant carbonization of low-molecular-weight biomass, which facilitates the synthesis of biochar with smaller particle sizes.

2.2. Synthesis of Rice Husk Biochar by Further Chemical Activation or Pyrolysis. To compare the properties of biochar synthesized by different methods, two other kinds of biochar were also synthesized by further chemical activation or a pyrolysis method. Specifically, the activation involves dissolving KOH in distilled water, mixing it with RSC, then drying it, and placing it in a tube furnace at 750 °C; the product was recorded as RSCK-750, and the whole process lasted for 9 h. The pyrolytic biochar was produced in a tube furnace by heating the rice husk to 750 °C in an N_2 atmosphere at a heating rate of 10 °C min^{-1} and then milling it into powder, denoted as RH-750. The whole process lasted for 8 h.

2.3. Synthesis of Biochar Carrier-Based SCR Catalysts. Our previous studies showed that the optimum loading of Mn transition metal oxides on the surface of biochar is 10 wt %.[37] The RSC, RSCK-750, and RH-750 were impregnated in a mixed aqueous solution of $Mn(NO_3)_2$ and $Ce(NO_3)_3$ (molar ratio = 2:1) and then were ultrasonically oscillated with power of 400 W and frequency of 40 kHz for 3 h at ordinary temperature and dried at 80 °C for 24 h. Finally, the dried samples were placed in a tube furnace and heated to 500 °C at a rate of 10 °C min^{-1} under N_2 conditions for 2 h. The SCR

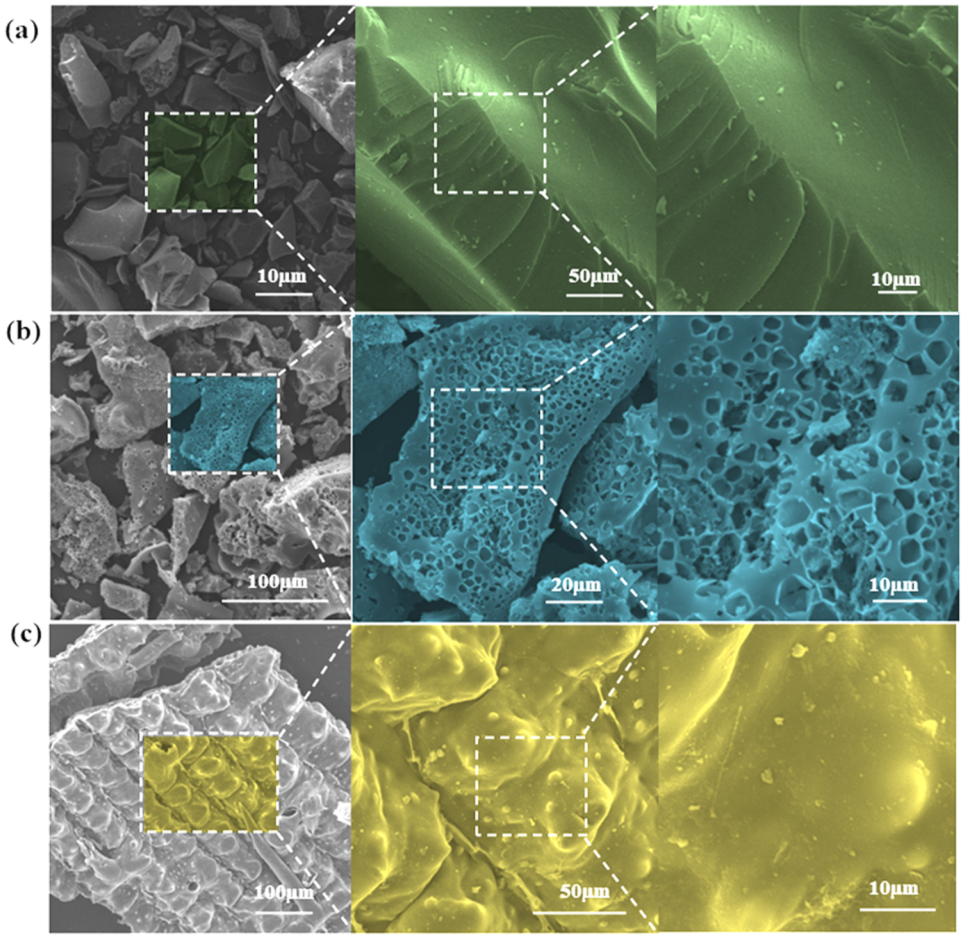

Figure 3. SEM images of different rice husk biochars: (a)RSC; (b)RSCK-750; and (c)RH-750.

https://doi.org/10.1021/acsomega.5c04370
ACS Omega XXXX, XXX, XXX−XXX

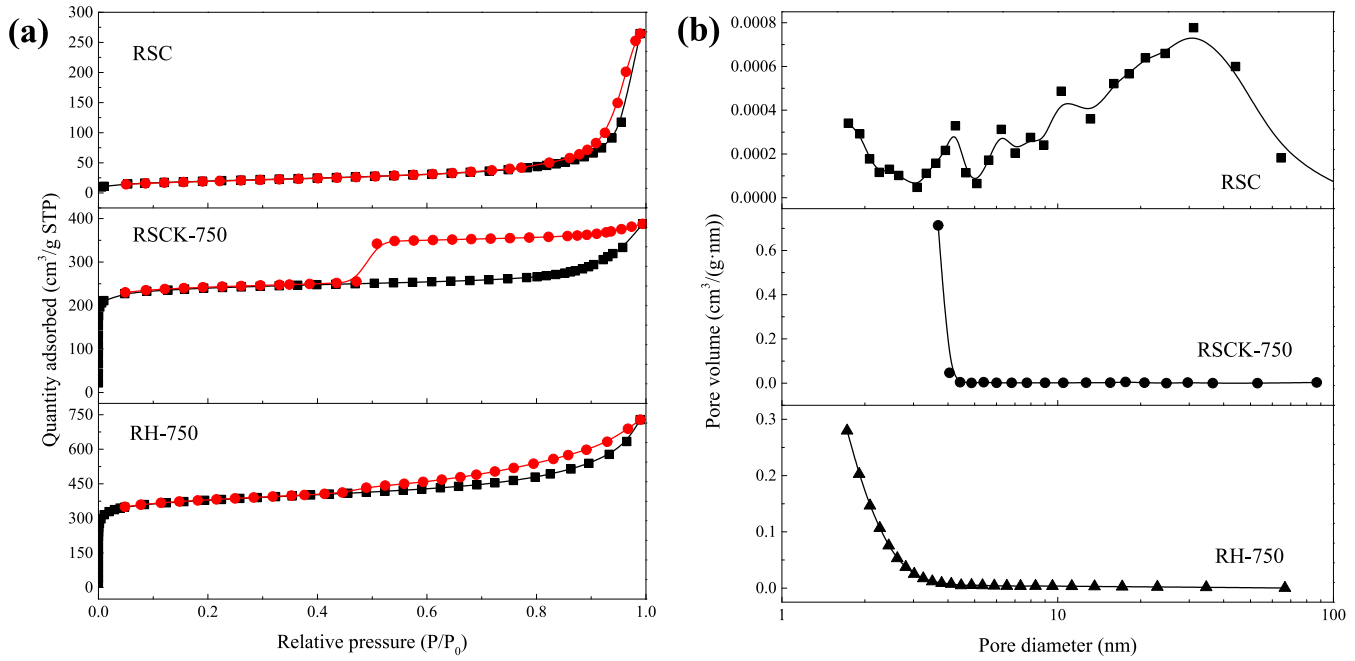

Figure 4. (a) N_2 adsorption−desorption isotherms and (b) pore size distribution of different catalysts.

Table 1. Physical Characteristics of the Rice Husk Biochar

sample	BET surface area/(m^2/g)	pore diameter/(nm)	pore volume/(cm^3/g)
RSC	38.2	7.4	0.091
RSCK-750	715.17	2.82	0.269
RH-750	400.09	2.54	0.128

catalysts were labeled as Mn−Ce/RSC, Mn−Ce/RSCK-750, and Mn−Ce/RH-750, respectively.

2.4. Characterization. The surface morphology of the experimental samples was observed by a scanning electron microscope; the isotherms of the products were determined by nitrogen adsorption−desorption instrument, and the physical composition of the samples was scanned by X-ray diffractometer.

For testing the catalytic activity, 0.2 g of the catalyst was weighed and placed in a fixed bed reactor. A flue gas mixture consisting of NO, NH_3, and O_2 was used as a simulated flue gas with a total gas stream of 130 mL min^{-1} (400 ppm of NO, 400 ppm of NH_3, 5 vol % O_2, equilibrated with N_2). The test temperature range was from 80 to 260 °C, and the gas time-space velocity (GHSV) was 15000 h^{-1}. The denitrification efficiency of the catalyst was expressed in terms of NO conversion and was calculated using the following formula

$$\text{NO conversion}(\%) = \frac{C_0 - C}{C_0} \times 100\%$$

where C_0 represents the inlet NO gas concentration (ppm) and C represents the outlet NO gas concentration (ppm).

3. RESULTS AND DISCUSSION

3.1. Morphology. RSC, RSCK-750, and RH-750 were all made from rice husk as the carbon source, and their morphologies are shown in Figure 3. It shows that RSC has a smooth blocky surface without pore structure, while RSCK-750 exhibits a homogeneous and dense spongy pore structure, and RH-750 has a rippled surface with a uniformly distributed raised structure; no pore structure was observed.

The analysis of Figure 4 indicates that the prepared biomass-derived carbon material exhibits typical hierarchical microporous−mesoporous structure characteristics. The adsorption capacity rapidly increases in the low-pressure region (P/P_0 < 0.1), showing a type I curve feature, which indicates that the material has abundant micropores; a type H4 hysteresis loop appears in the medium-pressure region (P/P_0 = 0.4−0.8) with a relatively high closing pressure, confirming the existence of well-ordered mesopores in the carbon material. This unique microporous−mesoporous composite pore structure not only provides a large specific surface area but also forms efficient mass transfer channels, endowing it with potential application advantages in the field of catalysis. Furthermore, the specific surface area and pore structure parameters are shown in Table 1.

3.2. Structure of Biochar Carrier-Based SCR Catalysts. To investigate the effect of biochar on the physical phase structure of the catalyst components, catalysts were subjected to X-ray Diffraction (XRD) tests. As shown in Figure 5, the diffraction peaks of the samples at 26.6 and 42.5° correspond to the (002) crystallographic plane and (100) crystallographic plane of graphite (PDF#99−0057). After loading Mn−Ce metal oxides, the catalysts have similar characteristic peaks corresponding to Mn_2O_3 (PDF#33−0900), MnO_2 (PDF#39−0375), CeO_2 (PDF#34−0394), and Ce_2O_3 (PDF#49−1458), respectively. Mn−Ce/RSC and Mn−Ce/RH-750 have narrow diffraction peak widths, indicating that the active components of the metal oxides are unevenly distributed and internally agglomerated and that the crystal structure is dominant. After KOH activation, except for the diffraction peak of CeO_2, the diffraction peaks of the other metal oxides in Mn−Ce/RSCK-

https://doi.org/10.1021/acsomega.5c04370
ACS Omega XXXX, XXX, XXX−XXX

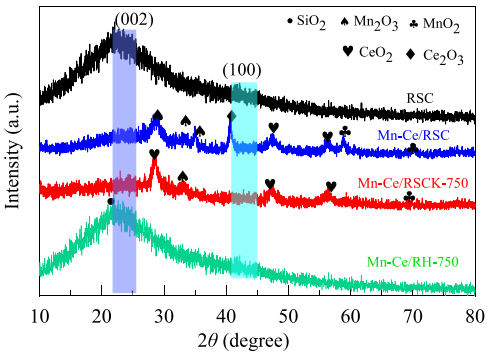

Figure 5. XRD spectra of biochar carrier-based SCR catalysts.

750 were relatively weakened, which indicated that the active components were dispersed internally or existed in an amorphous structure, and carrier of RSCK-750 was not conducive to the dispersion of CeO_2. In addition, the diffraction peak intensities belonging to both the (002) and (100) crystal planes were significantly weakened compared to RSC after loading Mn−Ce oxides, indicating that the doping of metal oxides affects the graphite microcrystalline structure, which may split it into small, irregular graphite flakes, thus leading to the changes in the peak intensities of the (002) and (100) crystal planes.[38]

3.3. Characterization of Catalysts. *3.3.1. Functional Groups on the Surface of Acid-Hydrolyzed Biochar Carrier-Based SCR Catalysts.* Fourier transform infrared spectroscopy (FTIR) tests were carried out on the three catalysts, as shown in Figure 6a. All of the catalysts have similar FTIR spectra; the adsorption bands around 3434 cm^{-1} were attributed to O−H stretching vibration, indicating the presence of carboxylic acid and hydroxyl group,[39] the adsorption bands around 1633 cm^{-1} belong to C═C stretching vibration,[40] and the adsorption bands around 1081 cm^{-1} belong to C−O stretching vibration.[41] After KOH activation, the intensity of peaks belonging to the polarizing group of O−H at 3434 cm^{-1} for Mn−Ce/RSCK-750 is larger than that of inactivated Mn−Ce/RSC and Mn−Ce/RH-750, and the peaks belonging to C═C and C−O at 1633 and 1081 cm^{-1}, respectively, are not significantly changed, indicating that KOH activation of acid-hydrolyzed biochar would introduce more O−H groups but has no obvious effect on the other two groups. This may be due to the fact that in the process of KOH-activated pyrolysis, KOH first reacted with oxygen-containing species in the biomass such as C═O, O−H, and C−O groups, releasing a large number of free radicals or hydrogen protons to form a large number of vacancies, and then −OH in KOH combined with these vacancies and formed new oxygen-containing groups in rice husk biochar.[42]

3.3.2. Compositional Valence of Elements on the Surface of Biochar-Based Carrier SCR Catalysts. The valence and composition of the elements on the surface of the biochar carrier-based catalysts were evaluated by X-ray photoelectron spectroscopy (XPS) testing, and the obtained profiles of the three catalyst samples are shown in Figure 6b. The presence of the elements Mn, Ce, and O was detected in the profiles of the three catalyst samples, and in order to determine the valence of each element on the surface of the catalyst samples, fine spectral scans were performed on Mn, Ce, and O, respectively.

The Mn 2p profile of the catalyst is shown in Figure 7, and the peak near 641.5 eV corresponds to the Mn $2p_{3/2}$. The three peaks obtained after the split-peak fitting process were Mn^{4+} (645.3 eV), Mn^{3+} (642.1 eV), and Mn^{2+} (640.5 eV), indicating that the Mn mainly exists in the form of MnO_2, Mn_2O_3, and MnO.[43] The relative atomic weights of Mn^{4+}/Mn^{n+}, Mn^{3+}/Mn^{n+}, and Mn^{2+}/Mn^{n+} in the catalyst samples are shown in Table 2. After KOH activation and pyrolysis, the Mn^{4+} content on the surface of Mn−Ce/RSCK-750 (23.2%) increased compared to that of Mn−Ce/RSC (20.4%), which could be attributed to KOH activation and pyrolysis, and the increase of SSA of the carbon material was favorable for the generation of Mn^{4+}. Mn^{4+} improved the adsorption of reactive gases on the active sites, and since it has a low temperature, Mn^{4+} could improve the adsorption of reactive gases at the active sites, and due to its good catalytic oxidation performance at low temperatures, it can promote the oxidation of NO and improve the denitrification activity of the catalyst.[44]

Figure 8 shows the Ce 3d maps of these three catalyst samples. After processing by split-peak fitting, the profile consists of eight parts: the peaks labeled u′ and v′ correspond to Ce^{3+}, and the remaining six peaks are attributed to Ce^{4+}.[45] The elemental valence percentages of Ce in the catalyst samples are listed in Table 3. The Ce^{3+} content on the surface of Mn−Ce/RSC without KOH activation is 26.3%, which is higher than that of Mn−Ce/RSCK-750 after KOH activation (14.9%), indicating that the use of KOH-activated pyrolyzed RSCK-750 as a carrier was not conducive to the generation of

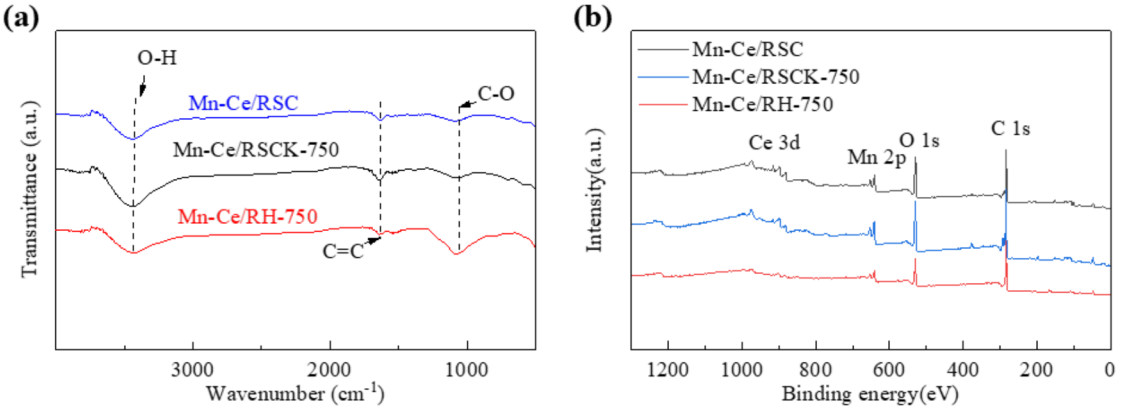

Figure 6. (a) FTIR spectra of rice husk biochar carrier-based SCR catalysts; (b) XPS spectrum of acid-hydrolyzed biochar carrier-based SCR catalysts.

https://doi.org/10.1021/acsomega.5c04370
ACS Omega XXXX, XXX, XXX−XXX

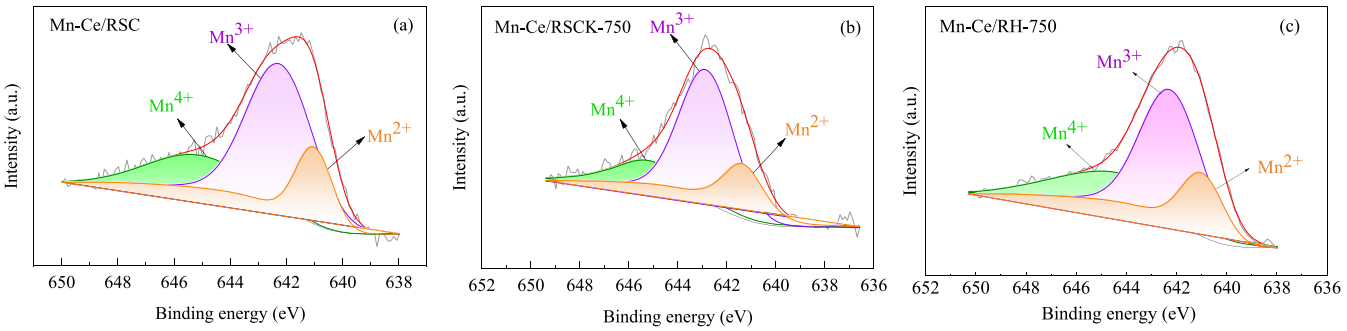

Figure 7. Mn 2p spectra of biochar carrier-based SCR catalysts: (a) Mn−Ce/RSC; (b) Mn−Ce/RSCK-750; and (c) Mn−Ce/RH-750.

Table 2. Relative Percentage of Valence Distribution of Mn Element in Biochar Carrier-Based SCR Catalysts

sample	Mn^{4+}/Mn^{n+}	Mn^{3+}/Mn^{n+}	Mn^{2+}/Mn^{n+}
Mn−Ce/RSC	20.4%	61.5%	18.1%
Mn−Ce/RSCK-750	23.2%	38.4%	38.4%
Mn−Ce/RH-750	25.7%	55.3%	19%

Table 3. Relative Percentage of Valence Distribution of Ce Element in Biochar Carrier-Based SCR Catalysts

sample	Ce^{3+}	Ce^{4+}
Mn−Ce/RSC	26.3%	73.7%
Mn−Ce/RSCK-750	14.9%	85.1%
Mn−Ce/RH-750	18.7%	81.3%

Ce^{3+}. The increase in the content of Ce^{3+} facilitates the enhancement of the number of unsaturated chemical bonds and the promotion of oxygen vacancy formation, which can enhance the oxygen migration ability, promote NO oxidation, and accelerate the process of the reaction.[46]

The O 1s profile of the catalyst was fitted to three peaks, as shown in Figure 9. The oxygen species with binding energy located around 530.1 eV corresponds to the catalyst surface lattice oxygen O_α, the oxygen species located near 531.7 eV is attributed to the catalyst surface chemisorbed oxygen O_β, and the oxygen species around 533.5 eV is the water adsorbed on the catalyst surface, which is noted as O_γ.[47] The relative percentages of oxygen species are listed in Table 4, and the Mn−Ce/RSC surface O_β content is 47.3%, which is higher than 34.6% for Mn−Ce/RSCK-750 and 27.6% for Mn−Ce/RH-750. Combined with the Ce 3d mapping, the higher percentage of Ce^{3+} on the surface of Mn−Ce/RSC may be responsible for the increase in its surface O_β content.[48] The O_β on the catalyst surface has a strong migration ability and thus higher activity and oxidation capacity than O_α and O_γ, which can promote the activation of NH_3 as well as the oxidation of NO and accelerate the reaction process.[49]

3.4. Denitrification Performance of Biochar Carrier-Based SCR Catalysts. The denitrification performance of the three biochar-based carried SCR catalysts was tested, and the results are shown in Figure 10. The maximum denitrification efficiency of 96.8 and 97.3% were obtained at 180 and 220 °C for Mn−Ce/RSC and Mn−Ce/RSCK-750, respectively, whereas the denitrification efficiency of the unactivated Mn−Ce/RH-750 at 240 °C was only 49.5%. Among them, Mn−Ce/RSC has a wider temperature window than Mn−Ce/RSCK-750 and Mn−Ce/RH-750 and achieves more than 90% denitrification efficiency in the range of 160−260 °C. Combined with the characterization results, the wider temperature window of Mn−Ce/RSC may be related to the increased content of Ce^{3+} and O_β; for Mn−Ce/RSCK-750, the higher denitrification efficiency than that of Mn−Ce/RSC in the range of 80−120 °C may be attributed to the large SSA and uniform mesoporous structure of Mn−Ce/RSC after KOH activation, which can promote the adsorption of reactive gases on the surface and the adsorption of Mn−Ce/RSCK-750 and Mn−Ce/RH-750 on the surface. The lowest denitrification efficiency of Mn−Ce/RH-750 is related to the uneven distribution of chemical components and the low Ce^{3+} and O_β contents on the surface. Therefore, compared with the biochar synthesized by pyrolysis, acid-catalyzed hydrolysis synthesized biochar, on the one hand, has the characteristics of simple operation and low energy consumption, and likewise in denitrification, it can achieve comparable effects with alkali activation treatment of acid-hydrolyzed biochar, which proves that acid hydrolysis is a promising and innovative synthesis method.

3.5. Byproducts of Acid-Hydrolyzed Rice Husk. During the acid hydrolysis process, except for the biochar, the filtered

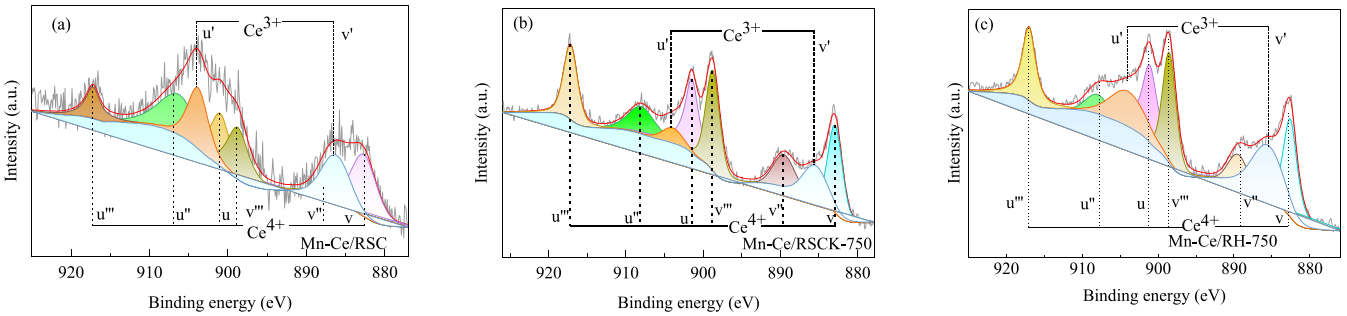

Figure 8. Ce 3d spectra of biochar carrier-based SCR catalysts: (a)Mn−Ce/RSC; (b)Mn−Ce/RSCK-750; and (c)Mn−Ce/RH-750.

https://doi.org/10.1021/acsomega.5c04370
ACS Omega XXXX, XXX, XXX−XXX

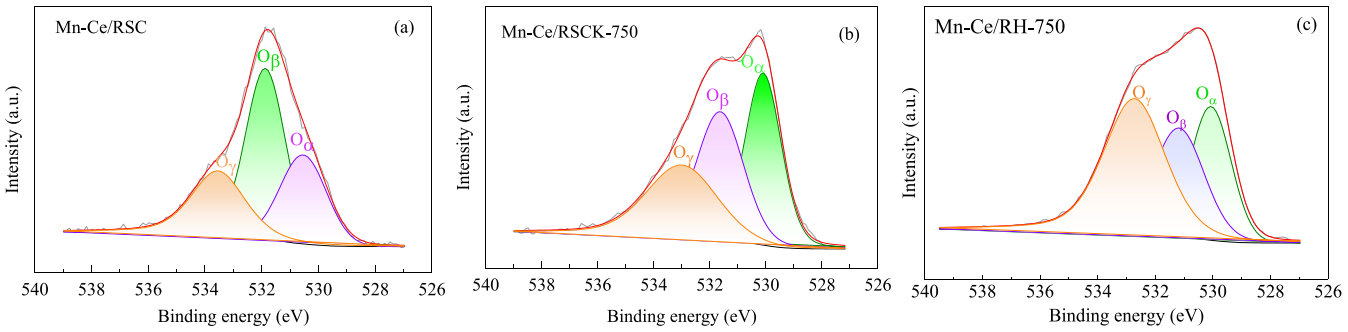

Figure 9. O 1s spectra of biochar carrier-based SCR catalysts: (a) Mn−Ce/RSC; (b) Mn−Ce/RSCK-75; and (c) Mn−Ce/RH-75.

Table 4. Relative Percentage of O Species in Biochar Carrier-Based SCR Catalysts

sample	O_α	O_β	O_γ
Mn−Ce/RSC	27.1%	47.3%	25.6%
Mn−Ce/RSCK-750	37.2%	34.6%	28.2%
Mn−Ce/RH-750	20.6%	27.6%	51.8%

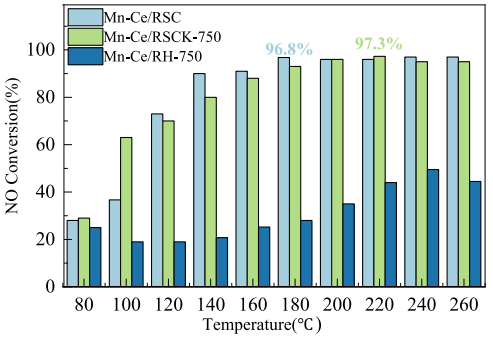

Figure 10. Denitrification performance of biochar carrier-based SCR catalysts.

residue is burned in a muffle furnace, which yields particles with a particle size of about 50 μm, named as RSF-800. To further determine the main composition of this byproduct RSF-800, the EDS energy spectrum of RSF-800 was scanned, as shown in Figure 11a,b.The EDS results showed that the main components of RSF-800 were Si and O elements. In order to further analyze the physical phase composition of RSF-800, it was tested and analyzed by XRD, as shown in Figure 11c. The XRD spectrum of RSF-800 showed a diffraction peak with a narrow peak width at 21.9°, corresponding to SiO_2 (PDF#29−0085), and no diffraction peaks of other species were detected, which indicated that the main composition of RSF-800 is SiO_2. SiO_2 powder has excellent high-temperature resistance, optoelectronic properties, and light transmittance and can be used in circuits, optical fibers, photovoltaics, and aerospace,[50] Thamri[51] et al. fabricated silicon solar cells using nickel oxide films on porous silicon and silicon substrates. SiO_2 was added as a carrier selective-passivation layer for porous silicon. The power conversion efficiency of the solar cell was as high as 19.52%.

4. CONCLUSIONS

In this work, biochar was successfully synthesized by acid-catalyzed hydrolysis at ordinary temperatures and pressures in a shorter time. Then, the biochar serves as a carrier for denitrification, yielding products with superior denitrification properties at low temperatures. The main conclusions are drawn as follows.

(1) Compared with pyrolyzed and further chemical-activated biochar, acid-catalyzed hydrolysis biochar was obtained in as little as 6 h, which enhances the overall reaction rate and achieves rapid synthesis of the product. In addition, the byproduct SiO_2 powder was obtained.

(2) Both Mn−Ce/RSC and Mn−Ce/RSCK-750 showed remarkable denitrification performance, reaching 96.8 and 97.3% at 180 and 220 °C, respectively, while that of Mn−Ce/RH-750 at 240 °C was only 49.5%. Furthermore, the Mn−Ce/RSC showed the widest working temperature range and the best activity at low temperatures.

(3) The wider temperature window of Mn Ce/RSC may be attributed to the increased content of Ce^{3+} and O_β content. For Mn−Ce/RSCK-750, its superior denitrifi-

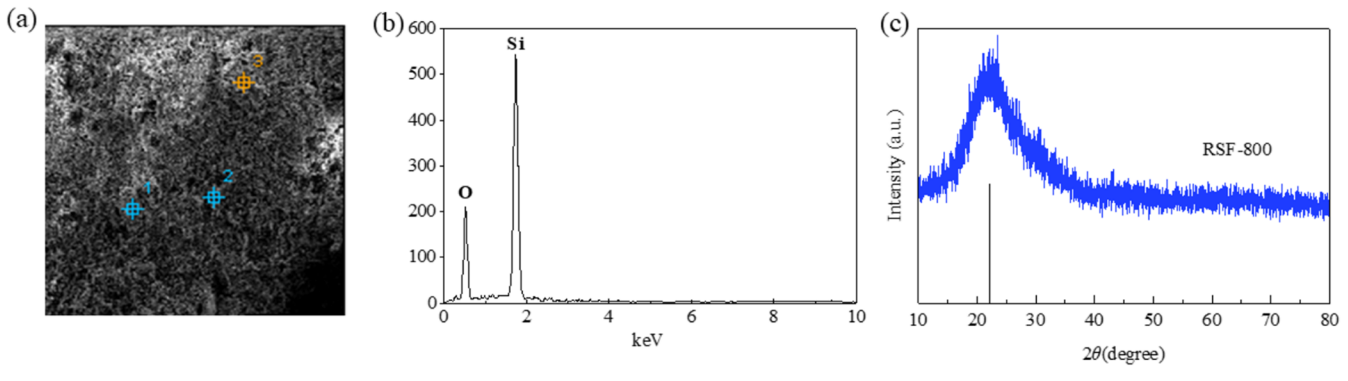

Figure 11. Acid hydrolysis of rice husk biochar byproduct RSF-800: (a, b) EDS energy spectra; (c) XRD spectra.

https://doi.org/10.1021/acsomega.5c04370
ACS Omega XXXX, XXX, XXX−XXX

cation efficiency within the 80−120 °C range compared to Mn−Ce/RSC can be ascribed to its larger specific surface area (SSA) and a uniform mesoporous structure, which was achieved post-KOH activation. This enhancement facilitates the adsorption of reactive gases on its surface. Conversely, the lowest denitrification efficiency of Mn−Ce/RH-750 is associated with the uneven distribution of active components and the scarcity of surface Ce^{3+} and O_β content.

AUTHOR INFORMATION

Corresponding Authors

Junchao Xu − *School of Energy and Environment, Anhui University of Technology, 243002 Maanshan, P. R. China*; orcid.org/0000-0002-1179-741X; Email: junchxu@ahut.edu.cn

Yiming Xie − *School of Energy and Environment, Anhui University of Technology, 243002 Maanshan, P. R. China*; Email: yiming_xx@163.com

Authors

Fan Li − *School of Energy and Environment, Anhui University of Technology, 243002 Maanshan, P. R. China*; orcid.org/0009-0006-9444-8536

Qingdong Yao − *School of Energy and Environment, Anhui University of Technology, 243002 Maanshan, P. R. China*

Fangyue Hu − *School of Energy and Environment, Anhui University of Technology, 243002 Maanshan, P. R. China*

Li Lv − *College of Mechanical and Electrical Engineering, China Jiliang University, 310018 Hangzhou, Zhejiang, P. R. China*

Huaqiang Chu − *School of Energy and Environment, Anhui University of Technology, 243002 Maanshan, P. R. China*; orcid.org/0000-0001-7399-5887

Complete contact information is available at: https://pubs.acs.org/10.1021/acsomega.5c04370

Author Contributions

F.L. wrote the manuscript and processed and reviewed the data. J.C.X. conducted the experiments and reviewed the manuscript. Y.M.X. wrote the manuscript and processed and reviewed the data. Q.D.Y. assisted in revising the manuscript. F.Y.H. assisted in processing the data. L.L. performed image modification. H.Q.C. performed an overall holistic review of manuscripts and data.

Notes

The authors declare no competing financial interest.

ACKNOWLEDGMENTS

This work was supported by the National Natural Science Foundation of China (52406121, 52176095), the Natural Science Foundation of Anhui province [2308085ME189, 2408085QE165], and the Opening Project of Engineering Technology Research Center of Anhui Education Department for Energy Saving and Pollutant Control in metallurgical process [GKF20-4].

REFERENCES

(1) Mondal, I.; Halder, P.; Kundu, M.; Paul, B. K.; Biswas, S.; Pal, A.; Sau, S.; Mondal, D.; Paul, P. K.; Das, S. Energy-efficient sintering-free Chemically synthesized carbon nanofibers for high-performance supercapacitors. *Mater. Today Chem.* **2024**, *35*, No. 101905.

(2) Paukov, M.; Kramberger, C.; Begichev, I.; Kharlamova, M.; Burdanova, M. Functionalized fullerenes and their applications in electrochemistry, solar cells, and nanoelectronics. *Materials* **2023**, *16*, No. 1276.

(3) Aliyeva, S. Covalent carbon nanotube and fullerene hybrid structures: mini review. *Surf. Rev. Lett.* **2023**, *30*, No. 2330008.

(4) Li, Q. L.; Shan, R.; Zhang, J.; Lei, M.; Yuan, H. R.; Chen, Y. Enhancement of hydrogen and carbon nanotubes production from hierarchical Ni/ZSM-5 catalyzed polyethylene pyrolysis. *J. Anal. Appl. Pyrol.* **2023**, *169*, No. 10582.

(5) Zhang, J.; Zhang, Y.; Zhao, W.; Li, Z.; Zang, L. Facile fabrication of calcium-Doped carbon for efficient phosphorus adsorption. *ACS Omega* **2021**, *6* (1), 327−339.

(6) Jin, G.; Zhou, Q.; Duan, Z.; Shen, K.; Dong, Z.; Deng, S.; Yang, P. Multistage template-oriented design and tailoring of the hierarchical porous biocarbon materials for high-performance supercapacitors. *ACS Omega* **2024**, *9* (48), 47557−47566.

(7) Li, S.; Song, Y.; Xu, L.; Wang, J.; Yang, Z.; Zhao, Y.; Chen, F.; Liu, B.; Liu, L.; Chen, D.; Jiao, X. Functional electrospun nanofibrous hybrid materials for colorimetric sensors: a review. *ACS Omega* **2024**, *9* (5), 5157−5174.

(8) Doğan, H.; Taş, M.; Meşeli, T.; Elden, G.; Genc, G. Review on the applications of biomass-derived carbon materials in vanadium redox flow batteries. *ACS Omega* **2023**, *8* (38), 34310−34327.

(9) Puettmann, M.; Sahoo, K.; Wilson, K.; Oneil, E. Life cycle assessment of biochar produced from forest residues using portable systems. *J. Cleaner Prod.* **2020**, *250*, No. 119564.

(10) Xu, J. C.; Xie, Y. M.; Yao, Q. D.; Lv, L.; Chu, H. Q. Advances in sustainable nano-biochar: precursors, synthesis methods and applications. *Nanoscale* **2024**, *16*, 15009−15032.

(11) Gao, Y.; Han, F. Q.; Li, Y. H.; Qin, X.; Li, D.; Wu, Q.; Lin, G.; Zhang, X.; He, M. Supported catalysts derived from cobalt phyllosilicates for chemical vapor deposition growth of single-walled carbon nanotubes. *Carbon* **2023**, *215*, No. 118491.

(12) Larionov, K. B.; Povalyaev, P. V.; Kaltaev, A.Zh.; Slysarsky, K. V.; Gorshkov, A. S.; Gubin, V. E.; Stoyanovskii, V. O.; Pak, A.Ya. Electric arc gasification of pyrolysis oil with the production of hydrogen-enriched synthesis gas and carbon nanomaterial. *Fuel Process. Technol.* **2023**, *245*, No. 107746.

(13) Hu, L. Y.; Lu, Z. H.; Chen, F.; Zhang, J.; Xia, Y.; Zhang, W.; Gan, Y.; He, X.; Song, W.; Huang, H. Supercritical-assisted ball-milling synthesis of multicomponent Si/Fe_3O_4/C composites for outstanding lithium-storage capability. *Energy Fuels* **2023**, *37*, 8042−8050.

(14) Omoriyekomwan, J. E.; Tahmasebi, A.; Dou, J. X.; Wang, R.; Yu, J. A review on the recent advances in the production of carbon nanotubes and carbon nanofibers via microwave-assisted pyrolysis of biomass. *Fuel Process. Technol.* **2021**, *214*, No. 106686.

(15) Li, L.; Jiang, Y. L.; Guo, C.; Han, K.; Cui, X.; He, C.; Chen, Y.; Yang, Y. Mechanochemical production of graphene/amorphous carbon/Mn_3O_4 nanocomposites for asymmetric supercapacitor. *Appl. Surf. Sci.* **2024**, *653*, No. 159388.

(16) Gaykwad, B.; Thakur, A.; Buch, A.; Jasuja, K. Large-scale synthesis of electrochemically active titanium diboride-based nanosheets by high-energy ball milling. *J. Phys. Chem. C* **2023**, *127*, 15887−15900.

(17) Titirici, M. M.; White, R. J.; Brun, N.; Budarin, V. L.; Su, D.; Monte, F.; Clark, J. H.; MacLachlan, M. J. Sustainable carbon materials. *Chem. Society Rev.* **2015**, *44*, 250−290.

(18) Yang, X. W.; Ma, W. H.; Wei, K. X.; Chen, Z. J.; Yang, X.; Dong, Y. Q. Preparation and characterization of high performance biomass char reductant. *Chin. J. Process Eng.* **2016**, *16*, 330−333.

(19) Madhu, R.; Periasamy, A. P.; Schlee, P.; Hérou, S.; Titirici, M. M. Lignin: A sustainable precursor for nanostructured carbon materials for supercapacitors. *Carbon* **2023**, *207*, 172−197.

(20) Liu, Y.; Liu, J. Q.; Song, P. A. Recent advances in polysaccharide-based carbon aerogels for environmental remediation and sustainable energy. *Sustainable Mater. Technol.* **2021**, *27*, No. e0024.

(21) Meng, X. T.; Li, Z. Y.; Li, D.; Huang, Y.; Ma, J.; Liu, C.; Peng, X. Efficient base-free oxidation of monosaccharide into sugar acid under mild conditions using hierarchical porous carbon supported gold catalysts. *Green Chem.* **2020**, *22*, 2588−2597.
(22) Wang, J.; Zhang, P. X.; Liu, L.; Zhang, Y.; Yang, J.; Zeng, Z.; Deng, S. Controllable synthesis of bifunctional porous carbon for efficient gas-mixture separation and high-performance supercapacitor. *Chem. Eng. J.* **2018**, *348*, 57−66.
(23) Zhang, H.; Sun, Q. D.; He, Q.; Zhang, Y.; He, X.; Gan, T.; Ji, H. Single Cu atom dispersed on S, N-codoped nanocarbon derived from shrimp shells for highly-efficient oxygen reduction reaction. *Nano Res.* **2022**, *15*, 5995−6000.
(24) Guo, C. Z.; Liao, W. L.; Li, Z. B.; Chen, C. Exploration of the catalytically active site structures of animal biomass-modified on cheap carbon nanospheres for oxygen reduction reaction with high activity, stability and methanol-tolerant performance in alkaline medium. *Carbon* **2015**, *85*, 279−288.
(25) Moraes, C. A. M.; Fernandes, I. J.; Calheiro, D.; Kieling, A. G.; Brehm, F. A.; Rigon, M. R.; Filho, J. A. B.; Schneider, I. A. H.; Osorio, E. Review of the rice production cycle: by-products and the main applications focusing on rice husk combustion and ash recycling. *Waste Manage. Res.* **2014**, *32*, 1034−1048.
(26) Kong, X.; Zhu, Y. F.; Lei, H. W.; Wang, C.; Zhao, Y.; Huo, E.; Lin, X.; Zhang, Q.; Qian, M.; Mateo, W.; Zou, R.; Fang, Z.; Ruan, R. Synthesis of graphene-like carbon from biomass pyrolysis and its applications. *Chem. Eng. J.* **2020**, *399*, No. 125808.
(27) Huang, B. B.; Liu, Y. C.; Xie, Z. L. Two dimensional nanocarbons from biomass and biological molecules: synthetic strategies and energy related applications. *J. Energy Chem.* **2021**, *54*, 795−814.
(28) Huo, Y.; Xiu, S. J.; Meng, L. Y.; Quan, B. Solvothermal synthesis and applications of micro/nano carbons: A review. *Chem. Eng. J.* **2023**, *451*, No. 138572.
(29) Kosheleva, R. I.; Mitropoulos, A. C.; Kyzas, G. Z. Synthesis of activated carbon from food waste. *Environ. Chem. Lett.* **2019**, *17*, 429−438.
(30) Jiang, B.; Cao, L.; Yuan, Q.; et al. Biomass straw-derived porous carbon synthesized for supercapacitor by ball milling. *Materials* **2022**, *15*, No. 924.
(31) Song, M.; Tang, X.; Xu, J.; Yu, L.; Wei, Y. The formation of novel carbon/carbon composite by chemical vapor deposition: An efficient adsorbent for enhanced desulfurization performance. *J. Anal. Appl. Pyrol.* **2016**, *118*, 34−41.
(32) Zhang, M. M.; Dong, Z.; Fang, L. T.; Zhi, C.; Dong, H. R.; Ke, Z. X.; Liu, J.; Yu, L. J. Hydrothermal carbonization of size-controlled carbon microspheres from waste disposable towel with correlation analyze. *Diamond Relat. Mater.* **2023**, *139*, No. 110395.
(33) Zhang, J.; Tahmasebi, A.; Omriyekomwan, J. E.; Yu, J. L. Direct synthesis of hollow carbon nanofibers on bio-char during microwave pyrolysis of pine nut shell. *J. Anal. Appl. Pyrol.* **2018**, *130*, 142−148.
(34) Zheng, Z.; Zhao, B.; Guo, Y.; Guo, Y. J.; Pak, T.; Li, G. T. Preparation of mesoporous batatas biochar via soft-template method for high efficiency removal of tetracycline. *Sci. Total Environ.* **2021**, *787*, No. 14739.
(35) Hou, J. Z.; Mao, X. Y.; Wang, J. Y.; Liang, C.; Liang, J. Preparation of rice husk-derived porous hard carbon: A self-template method for biomass anode material used for high-performance lithium-ion battery. *Chem. Phys.* **2021**, *551*, No. 11135.
(36) Tito, E.; Pipitone, G.; Monteverde Videla, A. H. A.; Bensaid, S.; Pirone, R. Exploring HTL pathways in carbohydrate−protein mixture: a study on glucose−glycine interaction. *Biomass Convers. Biorefin.* **2023**, *13*, 16385−16404.
(37) Xu, J. C.; Liu, H. X.; Sun, Y. L.; Chu, H.; Lv, L.; Zheng, Z.; Wu, Y. Promotion of catalytic performance of Mn−Ce/biochar catalysts in SCR reaction by ultrasonic treatment. *J. Energy Institute* **2022**, *102*, 350−361.
(38) Yang, J.; Ren, S.; Zhang, T. S.; et al. Iron doped effects on active sites formation over activated carbon supported Mn-Ce oxide catalysts for low-temperature SCR of NO. *Chem. Eng. J.* **2020**, *379*, No. 122398.
(39) Thompson, J. G.; Gao, X.; Toma, S.; et al. Decomposition of N-nitrosamines formed in CO_2 capture systems through electrochemically-mediated reduction on carbon xerogel electrode. *Int. J. Greenhouse Gas Control* **2019**, *83*, 83−90.
(40) Dai, F. W.; Zhuang, Q. Y.; Huang, G.; et al. Infrared spectrum characteristics and quantification of OH groups in coal. *ACS Omega* **2023**, *8*, 17064−17076.
(41) Praveena, B.; Sivanesan, T.; Kanagathara, N.; Ranjani, R.; Janczak, J.; Senthilkumar, K. Growth, structural, spectral, optical, thermal, third-order nonlinear optical characteristics, and DFT studies of morpholinium trichloroacetate-Trichloroacetic acid co-crystals for potential optoelectronic applications. *Opt. Mater.* **2024**, *149*, No. 115066.
(42) Ye, C. P.; Huang, H. J.; Li, X. H.; et al. The oxygen evolution during pyrolysis of Hunlun Buir lignite under different heating modes. *Fuel* **2017**, *207*, 85−92.
(43) Wu, H. L.; He, M. Y.; Liu, W. Z.; Jiang, L.; Cao, J.; Yang, C.; Yang, J.; Peng, J.; Liu, Y.; Liu, Q. Application of manganese-containing soil as novel catalyst for low-temperature NH_3-SCR of NO. *J. Environ. Chem. Eng.* **2021**, *9*, No. 105426.
(44) Niu, Y.; Shang, T.; Hui, S.; Zhang, X.; Lei, Y.; Lv, Y.; Wang, S. Synergistic removal of NO and N_2O in low-temperature SCR process with MnOx/Ti based catalyst doped with Ce and V. *Fuel* **2016**, *185*, 316−322.
(45) Bai, B. Y.; Li, J. H.; Hao, J. M. 1D-MnO_2, 2D-MnO_2 and 3D-MnO_2 for low-temperature oxidation of ethanol. *Appl. Catal., B* **2015**, *164*, 241−250.
(46) Boningari, T.; Ettireddy, P. R.; Somogyvari, A.; Liu, Y.; Vorontsov, A.; McDonald, C. A.; Smirniotis, P. G. Influence of elevated surface texture hydrated titania on Ce-doped Mn/TiO_2 catalysts for the low-temperature SCR of NOx under oxygen-rich conditions. *J. Catal.* **2015**, *325*, 145−155.
(47) Liu, C. X.; Han, J. F.; Bi, Y. L.; Wang, J.; Guo, M.; Liu, Q. A novel Cerium-Tin composite oxide catalyst with high SO_2 tolerance for selective catalytic reduction of NOx with NH_3. *Catal. Today* **2021**, *376*, 65−72.
(48) Selvaraj, A. R.; Muthusamy, A.; Cho, I.; Kim, H. J.; Senthil, K.; Prabakar, K. Ultrahigh surface area biomass derived 3D hierarchical porous carbon nanosheet electrodes for high energy density supercapacitors. *Carbon* **2021**, *174*, 463−474.
(49) Yang, Z. Y.; Huang, B. F.; Zhang, G. F.; Dai, M.; Wen, Z.; Li, W. Low-temperature Denitration Mechanism of NH_3-SCR over Fe/AC Catalyst. *J. Wuhan Univ. Technol.* **2023**, *38*, 475−484.
(50) Taheri-Behrooz, F.; Maher, B. M.; Shokrieh, M. M. Mechanical properties modification of a thin film phenolic resin filled with nano silica particles. *Comput. Mater. Sci.* **2015**, *96*, 411−415.
(51) Thamri, S.; Raouadi, M. H. Enhancement of NiO/Si solar cell by adding porous silicon and a silicon dioxide SiO_2 carrier selective layer. *Mater. Lett.* **2024**, *360*, No. 136002.

https://doi.org/10.1021/acsomega.5c04370
ACS Omega XXXX, XXX, XXX−XXX